AIP Journal of Applied Physics

Ge1- y Sn y (y = 0.01-0.10) alloys on Ge-buffered Si: Synthesis, microstructure, and optical properties

C. L. Senaratne, J. D. Gallagher, Liying Jiang, Toshihiro Aoki, D. J. Smith, J. Menéndez, and J. Kouvetakis

Citation: Journal of Applied Physics **116**, 133509 (2014); doi: 10.1063/1.4896788
View online: http://dx.doi.org/10.1063/1.4896788
View Table of Contents: http://scitation.aip.org/content/aip/journal/jap/116/13?ver=pdfcov
Published by the AIP Publishing

$Ge_{1-y}Sn_y$ ($y = 0.01$-0.10) alloys on Ge-buffered Si: Synthesis, microstructure, and optical properties

C. L. Senaratne,[1] J. D. Gallagher,[2] Liying Jiang,[2] Toshihiro Aoki,[3] D. J. Smith,[2] J. Menéndez,[2] and J. Kouvetakis[1]
[1]*Department of Chemistry and Biochemistry, Arizona State University, Tempe, Arizona 85287-1604, USA*
[2]*Department of Physics, Arizona State University, Tempe, Arizona 85287-1504, USA*
[3]*LeRoy Eyring Center for Solid State Science, Arizona State University, Tempe, Arizona 85287-1704, USA*

(Received 14 May 2014; accepted 18 September 2014; published online 2 October 2014)

Novel hydride chemistries are employed to deposit light-emitting $Ge_{1-y}Sn_y$ alloys with $y \leq 0.1$ by Ultra-High Vacuum Chemical Vapor Deposition (UHV-CVD) on Ge-buffered Si wafers. The properties of the resultant materials are systematically compared with similar alloys grown directly on Si wafers. The fundamental difference between the two systems is a fivefold (and higher) decrease in lattice mismatch between film and virtual substrate, allowing direct integration of bulk-like crystals with planar surfaces and relatively low dislocation densities. For $y \leq 0.06$, the CVD precursors used were digermane Ge_2H_6 and deuterated stannane SnD_4. For $y \geq 0.06$, the Ge precursor was changed to trigermane Ge_3H_8, whose higher reactivity enabled the fabrication of supersaturated samples with the target film parameters. In all cases, the Ge wafers were produced using tetragermane Ge_4H_{10} as the Ge source. The photoluminescence intensity from $Ge_{1-y}Sn_y$/Ge films is expected to increase relative to $Ge_{1-y}Sn_y$/Si due to the less defected interface with the virtual substrate. However, while $Ge_{1-y}Sn_y$/Si films are largely relaxed, a significant amount of compressive strain may be present in the $Ge_{1-y}Sn_y$/Ge case. This compressive strain can reduce the emission intensity by increasing the separation between the direct and indirect edges. In this context, it is shown here that the proposed CVD approach to $Ge_{1-y}Sn_y$/Ge makes it possible to approach film thicknesses of about 1 μm, for which the strain is mostly relaxed and the photoluminescence intensity increases by one order of magnitude relative to $Ge_{1-y}Sn_y$/Si films. The observed strain relaxation is shown to be consistent with predictions from strain-relaxation models first developed for the $Si_{1-x}Ge_x$/Si system. The defect structure and atomic distributions in the films are studied in detail using advanced electron-microscopy techniques, including aberration corrected STEM imaging and EELS mapping of the average diamond–cubic lattice. © *2014 AIP Publishing LLC*.
[http://dx.doi.org/10.1063/1.4896788]

I. INTRODUCTION

Recent interest in $Ge_{1-y}Sn_y$ alloys has been driven by the possibility of extending the infrared range of Ge-based telecom detectors,[1] by the accumulation of experimental evidence suggesting that the alloy becomes a direct gap material for modest Sn amounts,[2–4] and by the need to develop tensile stressors for future Ge-based CMOS technology.[5,6] Integration with Si technology would substantially expand the range of possible applications, and in this context the development of viable Chemical Vapor Deposition (CVD) routes to $Ge_{1-y}Sn_y$ films grown directly on Si substrates[7] represents an important milestone.

Similarly to Ge-on-Si epitaxy, the deposition of $Ge_{1-y}Sn_y$ on Si must overcome the difficulties posed by the 4% (and higher) lattice mismatch between film and substrate. To avoid island formation, growth must be initiated at very low temperatures, which introduces a very high density of defects. In the case of Ge, substantial improvements in film quality can be obtained by ramping up the growth temperatures and by applying high-temperature post-growth thermal annealings.[8–12] Unfortunately, these solutions are of limited value for the $Ge_{1-y}Sn_y$ system. Increases in growth temperature lead to lower Sn incorporation, and the temperature range for post-growth annealing is reduced by the possibility of Sn segregation.[13,14] These limitations reduce the ultimate film thickness that can be achieved and preclude the optimal elimination of defects, with considerable impact on the optical properties. In particular, optical emission can be strongly suppressed in thin, highly defected films. In Ge-like materials such as $Ge_{1-y}Sn_y$, film thickness is a particularly important consideration because the diffusion length of electron-hole pairs can be as high as 0.4 mm,[15,16] so that the non-radiative recombination velocity at the film/Si interface will affect the overall emission intensity. While reasonably good levels of photoluminescence and electroluminescence have been observed from $Ge_{1-y}Sn_y$ on Si,[4,17,18] these considerations suggest that there is significant room for improvement of these signals if the materials issues can be properly addressed.

The use of Ge buffer layers represents an intriguing approach for eliminating the disadvantages of direct growth on Si. The thermal robustness of Ge makes it possible to create relaxed, low defectivity Ge layers on Si, as described above, and these buffer layers can serve as virtual substrates for the growth of $Ge_{1-y}Sn_y$, thereby reducing the effective lattice mismatch to 1% or less for the Sn concentrations of interest. This is expected to reduce the defect concentration

in the $Ge_{1-y}Sn_y$ films. An additional advantage of using Ge buffer layers is that the predicted Type-I band alignment[19] between Ge and $Ge_{1-y}Sn_y$ would effectively confine the photoexcited electron-hole pairs to the $Ge_{1-y}Sn_y$ layer, far away from the highly defected Ge/Si interface. On the other hand, while the critical thickness for pseudomorphic growth of $Ge_{1-y}Sn_y$ on Si corresponds to a few atomic layers, all but insuring full strain relaxation in the growing film, the corresponding critical thickness value for growth on Ge is much higher,[20] raising the possibility of a substantial amount of compressive strain in the films. In fact, fully pseudomorphic $Ge/Ge_{1-y}Sn_y$ interfaces have been demonstrated by several groups.[20–25] While these interfaces are defect-free, compressive strain is undesirable because it increases the direct gap energy and the direct-indirect separation, suppressing the two key benefits of Sn alloying. Moreover, $Ge_{1-y}Sn_y$ films partially compressed or fully strained to Ge-buffer layers are of limited or no value as Ge stressors. Unfortunately, achieving high levels of strain relaxation in $Ge_{1-y}Sn_y$ layers grown on Ge or Ge-buffered Si has proven difficult because of the simultaneous requirements of preventing Sn segregation and maintaining a good surface morphology.[14,20]

In this paper, we report the CVD growth of thick ($\sim 1\ \mu m$), largely relaxed $Ge_{1-y}Sn_y$ layers on Ge-buffered Si. The Ge buffer layers are grown using the recently introduced tetragermane source, which leads to high structural perfection, and the $Ge_{1-y}Sn_y$ layers are deposited using digermane/stannane for $y \leq 0.06$ and trigermane/stannane for $y > 0.06$. The materials have an average strain relaxation of about 80% as grown. Even higher levels of strain relaxation can then be achieved using thermal treatments. The samples show a tenfold increase in photoluminescence intensity relative to $Ge_{1-y}Sn_y$/Si analogs, providing a striking experimental confirmation of the benefits of Ge-buffer layers.

The paper is structured as follows: first we describe the development of growth procedures to produce samples with Sn content between 1 and 10% Sn on Ge-buffered Si. Next, we present a detailed structural characterization of the grown layers, including an in-depth study of strain relaxation. This is followed by a Transmission Electron Microscopy (TEM) analysis in both plan view and cross sectional geometries. Further nanoscale analysis of the microstructure using Scanning TEM annular dark field (ADF) methods allows elucidation of the compositional dependence of both the density and type of defects. Atomic-column elemental mapping, based on EELS spectra at Ångstrom-scale resolution, are also applied to characterize bonding configurations and elemental distributions. Finally, we present photoluminescence results confirming the superior optical emission properties of these layers compared to similar films grown directly on Si buffer layers.

II. GROWTH AND ELEMENTAL CHARACTERIZATION

In this study, $Ge_{1-y}Sn_y$ films with $y = 1$–10% Sn are grown on Ge buffered Si using Ultra-High Vacuum CVD (UHV-CVD) of digermane (Ge_2H_6), trigermane (Ge_3H_8), and stannane (SnD_4). For the low-Sn content alloys between approximately 1% and 6% Sn we use reactions of Ge_2H_6 and SnD_4, while the higher concentration analogs of up to 10% Sn are produced using Ge_3H_8. The Ge_2H_6 approach was routinely applied in prior work to grow layers directly on Si with similar compositions, allowing the fabrication of the first generation of device prototypes, including photodetectors and light emitting diodes.[1,17] Films grown on Ge-buffered Si were found to have several improvements over those grown directly on Si. Using Ge buffer layers, the gas phase Ge/Sn ratios are approximately two times higher than those observed in the grown films. This is in contrast to depositions directly on Si, which required a several fold excess of the Ge-compound relative to the SnD_4 co-reactant. This development represents an advance from the point of view of process efficiency, reliability, and savings in sample production cost. Furthermore, the film thickness that can be achieved in growth on Ge is significantly larger than that on Si, presumably due to the reduced mismatch of the buffer with the film. However, when using Ge_2H_6 the growth rates tend to decrease with increasing Sn content above 6%, making it challenging to produce relaxed thick films with flat surfaces. Accordingly, to better grow these materials, we replaced Ge_2H_6 with Ge_3H_8, whose higher reactivity is more compatible with that of SnD_4, allowing depositions to occur with higher growth rates at the lower temperatures required to produce single-phase fully substitutional alloys.[26] Using this approach materials with Sn concentrations up to 10% were easily grown.

The Ge buffer layers employed in this study were grown on 4″ Si(100) high resistivity platforms via gas-source epitaxy of the single precursor Ge_4H_{10}. The resultant wafers were first characterized to ensure the highest possible crystal quality, thickness uniformity, and flat surface morphology, and then cleaved into four quadrants for subsequent use as substrates for deposition of the $Ge_{1-y}Sn_y$/Ge/Si(100) samples. The growth experiments were conducted in a UHV-CVD chamber using Ge_2H_6 procured from Voltaix Corp. and SnD_4 synthesized in our labs using literature methods. Stock mixtures were prepared by combining gaseous aliquots of the chemical reactants in a 3-L container in appropriate molar ratios that permit systematic control of the alloy stoichiometry. In most experiments, the amount of Ge_2H_6 in the mixture was kept constant in the range of 95–100 L-torr, while that of SnD_4 was varied from 1 to 6.5 L-Torr to achieve the desired elemental concentration reproducibly. The mixtures were then diluted with high-grade H_2. These formulations are designed to permit rigorous control of the mass flow during the reaction, yielding crystal layers with the desired thickness at viable growth rates. As noted above, a two-fold-excess of Ge_2H_6 relative to SnD_4 was found necessary to obtain the target alloy compositions. A possible mechanism that can account for the observation that only half of the Ge_2H_6 atoms delivered by the reaction mixture are being incorporated in the crystal is the dissociation reaction

$$Ge_2H_6 \rightarrow GeH_2 + GeH_4. \quad (1)$$

This dissociation produces highly reactive GeH_2 intermediates which then insert into the layer to deposit Ge via

complete desorption of H_2 byproducts. The reaction also produces an equal amount of GeH_4 molecules that are essentially unreactive at our low growth temperatures and are pumped away in the course of the experiment.

A similar procedure was followed for the preparation of reaction mixtures using Ge_3H_8. In this case, a constant amount of ~13 Torr of Ge_3H_8 was mixed in a 3 L container with appropriate quantities of SnD_4 ranging from 3–5 Torr to achieve the target Sn content from 6–10%. We note that a 25% excess of the Ge precursor was typically employed relative to SnD_4, in contrast to the 100% required for the Ge_2H_6 depositions described above. This result indicates that the Ge incorporation in the alloys is much more efficient using Ge_3H_8, as expected due to its higher reactivity as well as larger molecular mass and size.

In a typical CVD experiment, the substrates were dipped in HF/methanol to remove the surface oxide, rinsed in methanol and dried using a nitrogen nozzle. They were then inserted into the growth chamber under a constant flow of H_2 carrier gas maintained at 10^{-3} Torr under dynamic pumping while the reactor was heated at 300 °C using a resistance furnace. The H_2 background pressure was then increased to ~0.300 Torr and the furnace temperature was adjusted to the desired setting to establish deposition conditions. At this point, a 10% Ge_2H_6 mixture in H_2 was inserted into the reaction zone and allowed to flow over the substrates for 5 min to remove any residual impurities and generate a clean epitaxial surface. The reaction mixture was then introduced into the gaseous stream through a mass flow controller to initiate the crystal assembly. Under these conditions, $Ge_{1-y}Sn_y$ layers with $y = 0.01$–0.06 were deposited at temperatures between 350 and 315 °C, respectively, with a final thickness of 950–450 nm at a growth rate of 9–5 nm min^{-1}.

Rutherford Backscattering (RBS) was used to estimate the films thicknesses and measure the elemental composition of all samples. Figure 1 shows a representative 2 MeV random spectrum (black trace) featuring distinct peaks corresponding to the constituent Ge and Sn atoms. The concentrations were modeled using the program RUMP (Ref. 27), yielding, for the sample in the figure, 93% Ge and 7% Sn, respectively. The channeled spectrum (red trace) shows that the layer is a mono-crystalline single-phase material exhibiting a high degree of epitaxial alignment with the underlying substrate, as evidenced by the significantly reduced intensity of the channeled signal relative to the random counterpart.

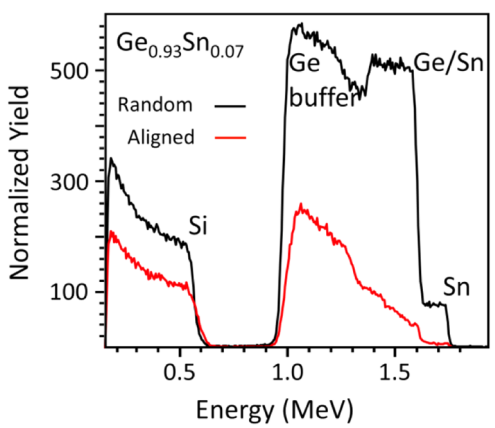

FIG. 1. RBS random and aligned spectra for a $Ge_{0.93}Sn_{0.07}$/Ge/Si(100) sample. The thickness of the top layer is 610 nm. The plots show distinct Ge and Sn signals corresponding to the buffer and the epilayer indicating a high degree of epitaxial alignment with the Si wafer. The ratio of aligned and random peak heights of the Sn signal in the spectrum is $\chi_{min} = 4.9\%$.

The interface sharpness was characterized using Electron Energy Loss Spectroscopy (EELS) with a probe size of 1.3 Å in STEM high angle annular dark field (HAADF) mode. Typical elemental maps were generated over large areas across the films encompassing a significant segment of the interface region. In all cases, the Ge and Sn maps showed that both elements appeared together in every atomic-scale region probed, without any indication of segregation of the individual constituents. Figure 2 shows the characteristic EELS map of Sn acquired from a $Ge_{0.96}Sn_{0.04}$/Ge thin specimen. The average Sn concentration profile obtained from a crystal with dimensions of 1.6 nm × 1.6 nm × 60 nm, in [110] projection, is indicated in a red-black scale. The dark area thus corresponds to the Ge buffer layer, where no measurable amounts of Sn above background levels are detected. The Sn map shows a sharp and well-defined transition of the atomic profile along the interface, indicating that no discernible Sn diffusion into the buffer has taken place. The above elemental map was then used to compute a series of line scans across the interface and average them over an area of 70 nm × 100 nm marked by the green box. This process generated a profile of the Sn content as a function of vertical distance, plotted on the right panel of Figure 2 for the $Ge_{0.96}Sn_{0.04}$ film. The fluctuations seen in the Ge region of the plot are characteristic of the data processing methods used to average the individual EELS spectra and represent the typical background noise level intrinsic to the technique. Assuming that the interface is Gaussian-broadened, with a standard deviation σ, the predicted

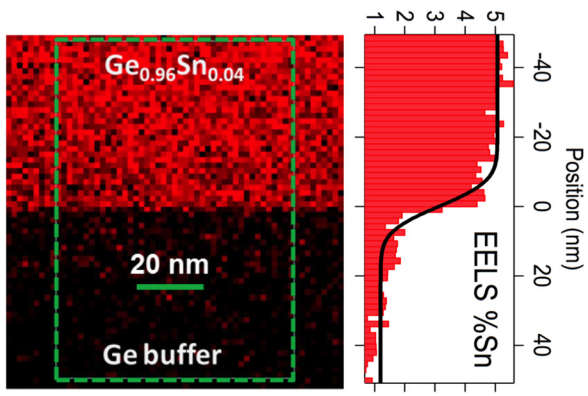

FIG. 2. STEM/EELS elemental map and concentration plots of a $Ge_{0.96}Sn_{0.04}$/Ge sample. The left panel shows Sn mapping profiles over a large film region across the interface. The red color denotes the presence of significant Sn concentrations whereas the black indicates only background levels of the atom. The right panel illustrates a quantitative composition profile indicating an approximate 4% Sn content in the sample, as expected. The latter profile was measured from a 70 nm × 100 nm area marked by the green box. The plot/map in this case shows highly uniform distributions of Sn atoms and a sharp, well-defined transition of Sn composition at the interface with the Ge buffer.

composition profile has the lineshape of a complementary error function. A fit with such a profile is shown as a solid line. It gives a broadening value $\sigma = 6.7$ nm and a step size of 3.87 ± 0.10, in very good agreement with the Sn concentration determined from RBS. The unique aspect of this type of analysis is that it incorporates an average of 50 or more lines scans across the interface (an individual line scan covers a 1.5 nm swath of material) and provides a more representative estimate of the lateral concentration average parallel to the interface plane. The sharp and abrupt transition in the composition profile across the GeSn/Ge boundary indicates that the interface plane is atomically smooth over a large area across the film.

III. HIGH-RESOLUTION X-RAY DIFFRACTION

High-Resolution X-Ray diffraction (HR-XRD) was used to determine the strain state and relaxed cubic lattice parameters of the films. Figure 3 shows representative examples of on axis 004 plots and 224 reciprocal space maps for a $Ge_{0.97}Sn_{0.03}$ sample grown at 335 °C and for more concentrated analogs grown at 310 °C ($Ge_{0.93}Sn_{0.07}$) and 295 °C ($Ge_{0.91}Sn_{0.09}$). From these spectra, we extract the lattice constants a and c parallel and perpendicular to the Ge/$Ge_{1-y}Sn_y$ interface, respectively. The relaxed cubic lattice constant a_0 of the alloy follows from a and c by straightforward application of elasticity theory, as in Ref. 28. The cubic lattice parameter was found to increase smoothly from 5.665 Å to 5.737 Å in the 1–10% Sn composition range, as expected.[28] The strain component parallel to the interface is defined as $\varepsilon = (a - a_0)/a_0$. The "as-grown" layers were found to exhibit varying amounts of residual compressive strains ($a < a_0$) from −0.05% to −0.25% depending on composition and growth temperature. The compressive nature of the strain is graphically indicated in Fig. 3, where the centroid of the 224 diffraction peak is *below* the solid black line, which corresponds to full relaxation ($a = a_0$). It is apparent from the figure that the Ge buffers exhibit a small amount of tensile strain. This is a well-known phenomenon due to mismatch of thermal expansion coefficients with the Si substrate.[29]

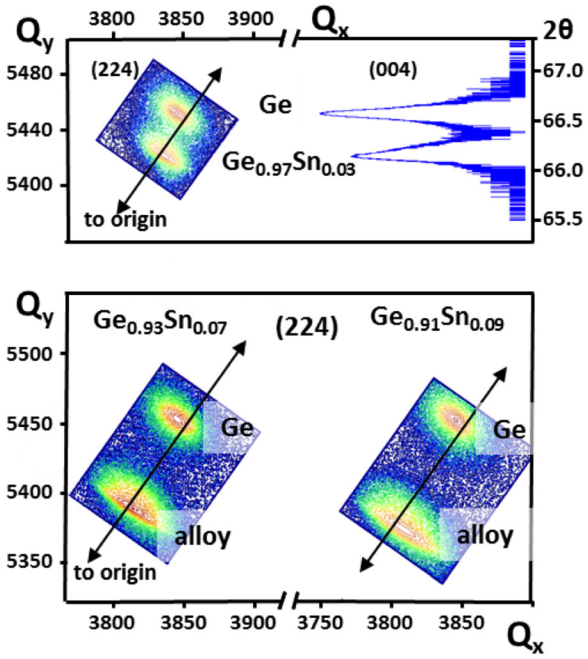

FIG. 3. (top) Representative XRD patterns of a $Ge_{0.97}Sn_{0.03}$/Ge material showing the 004 plots and 224 reciprocal space maps of the buffer and epilayer. The latter is virtually strain free (0.0636%) relative to Si and exhibits a cubic lattice constant of 5.688 Å. (bottom) Reciprocal space maps near the off-axis 224 reflection for samples with compositions $G_{0.93}Sn_{0.07}$ and $Ge_{0.91}Sn_{0.09}$. In both cases the position of the Ge peak is located above the cubic relaxation line, indicating that the buffer exhibits a slight tensile strain (~0.15%) induced by the thermal mismatch with the underlying Si platform. The corresponding alloy peaks fall slightly *below* the line, indicating the presence of residual compressive strains of 0.146% and 0.142%, respectively.

The XRD patterns of samples across the entire composition range produced in this study indicate that the crystallinity is superior to that of similar films grown directly on Si using the trigermane method. The full-width at half maximum (FWHM) of the on axis rocking curves is typically at least 3–4 times lower than observed for GeSn/Si. For example the FWHM of ~4.5–5% Sn alloys is approximately 0.150°, which should be compared with 0.7° for Si analogs. Furthermore, the peak profiles of the reciprocal space maps are markedly sharper and narrower due to reduction in mosaic spread with increasing thickness and crystallographic alignment. Moreover, the crystallinity of the samples grown on Ge buffers is comparable across the 3–9% Sn concentration range, while in the case of GeSn/Si the structural quality degrades significantly with Sn incorporation. This is corroborated with XTEM characterizations of the local microstructure using high-resolution methods, as described below.

We define the fraction of strain relaxation as $R = 1 - \varepsilon/\varepsilon_{max}$, where $\varepsilon_{max} = (a_{Ge} - a_0)/a_0$. This fraction is show in Fig. 4, and we see that the strain in the as-grown samples is largely relaxed. The residual compressive strain can be further reduced or eliminated by subjecting the samples to rapid thermal annealing (RTA) treatments. For example, the 7% Sn sample in Fig. 3 possessed an as-grown strain $\varepsilon = -0.10\%$, corresponding to a relaxation fraction $R = 0.88$. After three 2 s-RTA cycles between 550 °C–600 °C, the strain was reduced down to $\varepsilon = -0.05\%$, which implies $R = 0.94$, without any indication of phase segregation or roughening of the surface. In other samples, the relaxation after RTA exceeds 100%, indicating the appearance of tensile strain due to thermal-expansion mismatch.

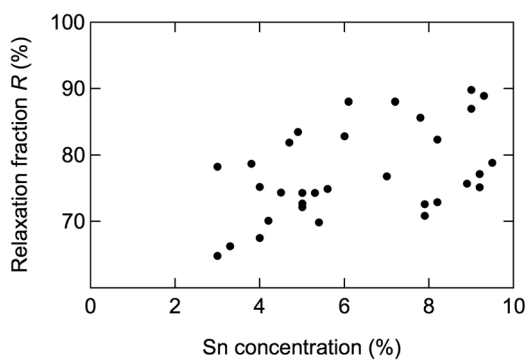

FIG. 4. Relaxation fraction R for as-grown $Ge_{1-y}Sn_y$ films on Ge-buffered Si.

To understand the high-level of relaxation, we computed the critical thickness h_c for growth of GeSn/Ge using standard Mathews-Blakeslee theory.[30] In the formulation used by Houghton,[31,32] the effective stress

$$\tau_{\text{eff}}(h) = \mu \cos\psi \left(\frac{1+\nu}{1-\nu}\right)\left[\varepsilon - \frac{K}{h}\ln\left(\frac{4h}{b}\right)\right] \qquad (2)$$

vanishes for $h = h_c$ and $\varepsilon = \varepsilon_{\max}$. Here, μ is the shear modulus, ν the Poisson ratio, b the Burger's vector magnitude, and ψ the angle between the sample surface and the normal to the slip plane. The dislocation-related constant in Eq. (2) is $K = (b/8\pi\cos\lambda)[(1-\nu\cos^2\beta)/(1+\nu)]$, where λ is the angle between the Burgers vector and the direction in the interface perpendicular to the dislocation line, and β the angle between the dislocation line and its Burgers vector. For 60° dislocations, for example, $\cos\beta = \cos\lambda = 1/2$, and $\cos\psi = (2/3)^{1/2}$.

The calculated h_c is shown as the solid black curve in Fig 5. The elastic parameters needed for the calculation were obtained by performing Voigt averages[33,34] of the elastic constants of Ge (Ref. 35) and α-Sn (Ref. 36). From these averages, we obtain for Ge a shear modulus $\mu = 56.1$ GPa, and a Poisson ratio $\nu = 0.200$, whereas for α-Sn we compute $\mu = 29.7$ GPa, and $\nu = 0.217$.

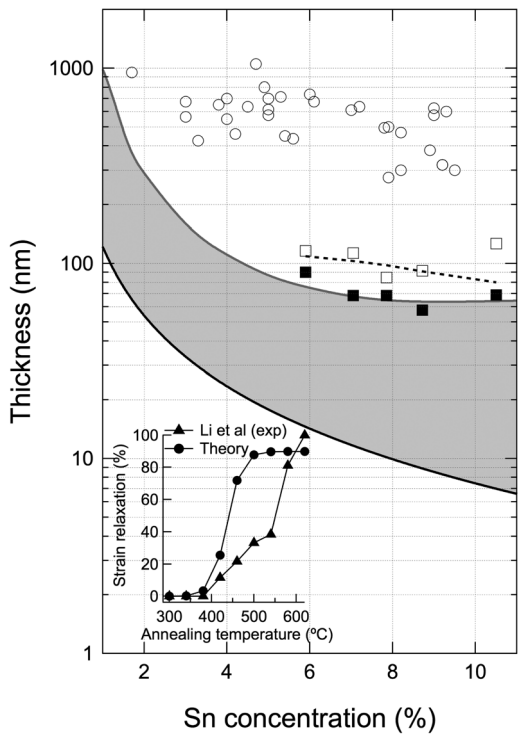

FIG. 5. $Ge_{1-y}Sn_y$ film thicknesses (empty white circles) compared with calculations of critical thickness for strain relaxation. The solid black line is a Mathews-Blakeslee calculation. Black squares correspond to fully strained samples reported by Gencarelli *et al.* (Ref. 20), and empty squares are the thicknesses of partially relaxed layers by the same authors. The dotted line corresponds to $|\varepsilon_{\text{dis}}| = 10^{-5}$ according to Houghton's kinetic relaxation model (Ref. 31). The parameters of the theory were adjusted to obtain a line between Gencarelli's fully strained and relaxed samples. When the same parameters are used to compute the thickness at which $|\varepsilon_{\text{dis}}| = 10^{-5}$ for the empty circle samples, the solid gray line is obtained. The gray area thus indicates the region of strain "metastability". All samples studied here are beyond this region, which explains their high level of strain relaxation. The inset shows the annealing-induced strain relaxation measured by Li *et al.* (Ref. 14) and the prediction from our model using the same parameters as in the simulation of strain relaxation during growth.

It is apparent from Fig. 5 that all of our samples exceed the critical thickness by at least one order of magnitude. However, since the growth temperatures are extremely low, the possibility of significant kinetic barriers to strain relaxation cannot be ruled out. In fact, Gencarelli *et al.* recently showed that fully strained $Ge_{1-y}Sn_y$/Ge samples can be fabricated with thicknesses that far exceed the Mathews-Blakeslee prediction.[20] These are shown as black squares in Fig. 5. The empty squares correspond to slightly thicker films—grown by the same authors—that show evidence of strain relaxation. Samples grown by Molecular Beam Epitaxy on Ge substrates are also found to be fully strained at thicknesses well in excess of the Mathews-Blakeslee curve.[37]

A phenomenological strain relaxation model was proposed by Hull *et al.* (Ref. 38) and systematically developed by Houghton to study $Ge_{1-x}Si_x$ alloys grown on Si.[31] The model assumes that the growth rate of the strain relaxation is proportional to the density n_{td} of dislocation threading segments times the dislocation velocity v, while threading dislocations are created at a rate j that is proportional to an initial density n_0 of incipient dislocation nuclei and pinned with probability η. The corresponding equations are

$$\frac{d\varepsilon_{\text{dis}}}{dt} = v n_{\text{td}} b \cos\lambda,$$
$$\frac{dn_{\text{td}}}{dt} = j - \eta v n_{\text{td}} \rho_{\text{md}}, \qquad (3)$$

where ρ_{md} is the length per unit area of the misfit segments at the epilayer/buffer interface. A detailed account of the model is given in Ref. 32. We have applied the same model to strain relaxation in $Ge_{1-y}Sn_y$/Ge. Houghton proposed Arrhenius expressions

$$j = B n_0 \left(\frac{\tau_{\text{eff}}}{\mu}\right)^n \exp\left(\frac{-Q_n}{k_B T}\right)$$
$$v = v_0 \left(\frac{\tau_{\text{eff}}}{\mu}\right)^m \exp\left(\frac{-Q_v}{k_B T}\right) \qquad (4)$$

for the dislocation nucleation rate and velocity. Here k_B is the Boltzmann constant and T the temperature in Kelvin. The parameters B, v_0, Q_n and Q_v are material constants independently determined from experiments on $Ge_{1-x}Si_x$ samples near the Si-rich end.[31] For pure Ge, detailed measurements of dislocation velocities were carried out by Yonenaga *et al.* (Ref. 39), whose recommended parameters v_0, n and Q_n are different from those proposed by Houghton. Since our samples are closer to pure Ge, we use the Yonenaga *et al.* results in our simulations. For the dislocation nucleation rate j, on the other hand, we are not aware of measurements on Ge-rich material, so we use the Houghton parameters.[31] The pinning probability was taken as $\eta = 1/12$ (Ref. 40). Thus the only adjustable parameter in this model is n_0, which is assumed to represent the density of heterogeneous incipient dislocation nuclei (particulates, interfacial

ledges and steps, etc.)[31] Recent results on $Ge_{1-x}Si_x$ layers on Si (Ref. 41) confirm the importance of heterogeneous nucleation. The strain relaxation produced by dislocations is $\varepsilon_{dis} = \varepsilon_{max} - \varepsilon$. The fit is carried out by computing the film thickness at which this strain relaxation reaches a value $|\varepsilon_{dis}| = 10^{-5}$, which is close to the limit of detectability using x-ray methods. The dotted line in Fig. 5, which gives this threshold thickness, was obtained using $n_0 = 7.3 \times 10^{11}\,cm^{-2}$ and the experimental growth rates from Gencarelli *et al.* (Ref. 42). Returning to our samples, we use the value of n_0 obtained from the fit to the samples in Ref. 20, combined with our growth rates and temperatures, to compute the thickness that satisfies the $|\varepsilon_{dis}| = 10^{-5}$ condition. This gives the solid grey line in Fig. 5. (To obtain a smooth curve, we adjusted a linear function of composition to the growth temperatures and growth rates, which gives a good empirical account of the data for all samples in Fig. 5). We see that the calculated line is well below the actual sample thicknesses, so that we predict an observable strain relaxation level for all of our samples, as found experimentally. In principle, the calculations can be continued beyond the solid line in Fig. 5 to predict the observed strain relaxation ε_{dis} at the actual sample thicknesses, but the values obtained are typically lower in magnitude than those observed. This is not surprising, since the model neglects dislocation multiplication, and therefore it can only be expected to be accurate at the initial stages of strain relaxation.

The value $n_0 = 7.3 \times 10^{11}\,cm^{-2}$ for the initial density of dislocation nuclei is orders of magnitude larger than the value found by Houghton ($n_0 = 5 \times 10^3\,cm^{-2}$) for growth of $Ge_{1-x}Si_x$ alloys on Si wafers at temperatures close to 500 °C, but comparable to the values found for $Ge_{1-x}Si_x$ films grown at temperatures near 300 °C, (Ref. 32) which are much closer to the growth temperatures of our $Ge_{1-y}Sn_y$ layers. One factor that may contribute to the large value of n_0 is the use of a Ge buffer grown on Si, since the unavoidable defects in the buffer layer may act as dislocation seeds in the $Ge_{1-y}Sn_y$ layers. To test this hypothesis, we grew $Ge_{1-y}Sn_y$ films directly on Ge substrates, and we find that films with thicknesses close to 500 nm and Sn concentrations around $y = 0.05$, well above the metastable relaxation line in Fig. 5, are still fully strained. This implies $n_0 < 3 \times 10^9\,cm^{-2}$. A full account of these growth experiments will be published elsewhere, but these initial results confirm that Ge-buffers on Si are a preferred platform if the goal is to obtain strain-relaxed $Ge_{1-y}Sn_y$ films. On the other hand, it should be stressed that a relatively small change in the poorly known activation energy for dislocation nucleation leads to significant changes in the values of n_0 obtained from the fit. A possible way to separate the contributions from n_0 and the nucleation activation energy is to apply the relaxation model to annealing experiments. Recently, Li and coworkers[14] reported detailed annealing studies of $Ge_{1-y}Sn_y$ layers grown by MBE. For fully strained $Ge_{0.92}Sn_{0.08}$ samples with a thickness of 160 nm, they found that films annealed for 40 s show the relaxation behavior shown as dark triangles the inset to Fig. 5. Using our relaxation model with exactly the same parameters, we predict the dark circles curve in the inset. We find that our model is unable to explain the sluggish observed relaxation, but it is in remarkable good agreement with the onset of observable relaxation, particularly if we take into account the fact that we are modeling samples grown by molecular beam epitaxy using parameters fit to samples grown by CVD. The results suggest that while the simple model does not fully capture the complexities of dislocation physics in $Ge_{1-y}Sn_y$ alloys, as will be discussed below, it is capable of reproducing the basic features of a diverse set of experiments based on a single set of parameters.

IV. DEFECT MICROSTRUCTURES

The structural properties of the samples were further characterized by transmission electron microscopy both in cross sectional (XTEM) and plan-view geometries to study the local microstructure and estimate the threading dislocation density in the bulk layer. Figure 6 shows an XTEM micrograph of a $Ge_{0.91}Sn_{0.09}$ film obtained with a JEM-4000EX high-resolution electron microscope operated at 400 keV with a resolution of 1.7 Å. Inspection of the Ge/$Ge_{0.91}Sn_{0.09}$ interface reveals occasional 60° dislocations and widely spaced short stacking faults penetrating down into the buffer layer rather than propagating through the bulk crystal. The latter is seen to be mostly devoid of threading defects and other types of structural imperfections arising from the high concentration of mismatched Sn atoms imbedded in the parent Ge lattice. Plan-view studies were conducted using the same microscope. Multiple micrographs taken from various samples showed intermittent dislocations evenly distributed throughout the $25 \times 25\,\mu m^2$ field of view of the experiment. The average areal density of these features for the 700 nm thick $Ge_{0.96}Sn_{0.04}$ in Fig. 7(a) was estimated to be in the range of $5 \times 10^7\,cm^{-2}$, which is substantially above the defect concentrations found for the Ge buffer layer using similar measurement protocols. A semi-quantitative estimate of the defect concentration appears to be on par with the average densities obtained

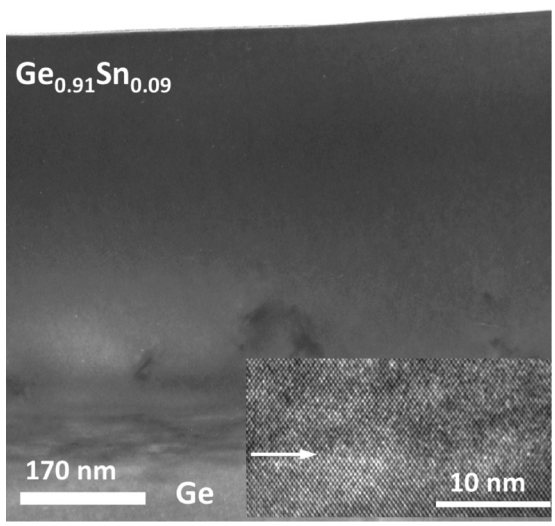

FIG. 6. XTEM micrograph of a 550 nm-thick $Ge_{0.91}Sn_{0.09}$ film grown on Ge-buffered Si. The image was obtained using a JEM-4000EX high-resolution electron microscope operated at 400 keV. The inset is a high-resolution image of the interface showing full commensuration of the lattice planes over an extended field of view.

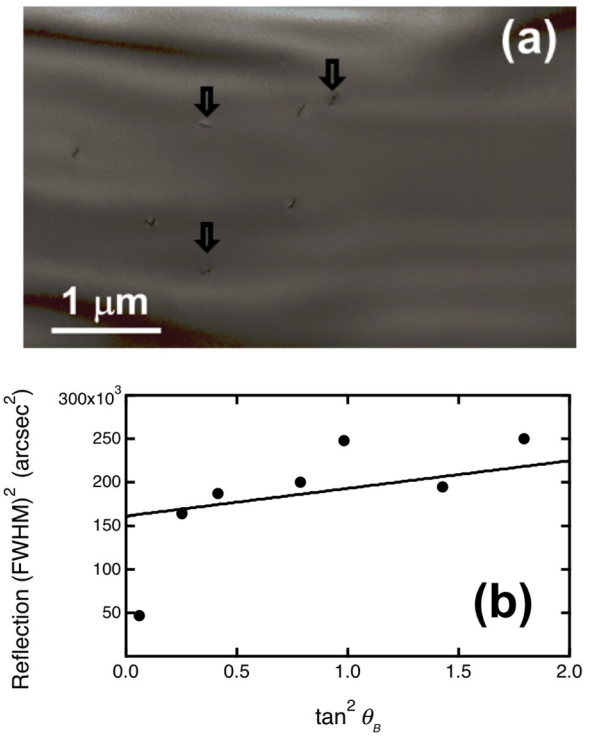

FIG. 7. (a) Plan view TEM image shows dislocations (examples marked by arrows) with an estimated density of $5 \times 10^7\,\mathrm{cm}^{-2}$. (b) Corrected FWHM of several Bragg reflections for a $Ge_{0.96}Sn_{0.4}$ sample. The solid line is a fit with Eq. (1), in which the dislocation density is the only adjustable parameter. The fit value is $n = (4.7 \pm 1.0) \times 10^8\,\mathrm{cm}^{-2}$.

from the cross-sectional view images, suggesting that our measurements may include some of these defects confined to the lower portion of the film along with those penetrating through to the top surface.

Ayers and coworkers[43,44] developed a methodology to extract the dislocation density n from the width of the x-ray rocking curves as a function of the Bragg angle. According to these authors, the full-width at half maximum (FWHM) β of a Bragg reflection, after correction for extinction, finite size, and specimen curvature, satisfies the equation

$$\beta^2 = K_\alpha(n) + K_\varepsilon(n)\tan^2\theta_B, \tag{5}$$

where θ_B is the Bragg angle, and the functions $K_\alpha(n)$ and $K_\varepsilon(n)$ depend on geometrical factors and the size of the Burgers vector. Explicit functional forms are given in Ref. 44. We have fit the width of our rocking curves in Fig. 7(b) with Eq. (5), using n as the single adjustable parameter, and we obtain $n = (4.7 \pm 1.0) \times 10^8\,\mathrm{cm}^{-2}$. Alternatively, since the determination of $K_\varepsilon(n)$ is affected by a large error due to the small range of Bragg angles in our experiments, we can equate $K_\alpha(n)$ to the square of the width of the (111) reflection, which has the smallest Bragg angle. Using this approach, we obtain $n = 1.5 \times 10^8\,\mathrm{cm}^{-2}$. Given the fact that only order-of-magnitude estimates can be expected from the x-ray method, as well as from the direct counting approach from the plan-view electron micrographs, the agreement between the two methods can be considered to be satisfactory.

To further investigate the local microstructure at the interface and identify the type and distribution of the dislocations generated under our reaction conditions we conducted atomic resolution experiments using a JEOL ARM 200 F microscope equipped with a STEM aberration corrector. STEM bright field (BF) images of the samples were acquired using a large collection angle (22 mrad), which enables atomic resolution as well as high contrast of interfaces and defects. Representative data are presented in Fig. 8 for a $Ge_{0.96}Sn_{0.04}$/Ge sample. Panel 8(a) reveals the presence of a smooth, uniform and crystalline film exhibiting sharp and well-defined hetero-interfaces. The dark contrast areas in panel 8(b) show the location of a stacking fault originating at the interface and penetrating through a short distance into the buffer layer rather than threading upwards into the film. These features represent the most common (most frequently visible) defects found at the interface of our materials and appear to be well separated from one another by a significant spacing of ~40 nm in the lateral direction, as shown in panel 8(c) for a pair pointing at different directions along 111 planes in 110 projection. In addition to stacking faults we also identified Lomer dislocations randomly distributed along the interface plane, shown as dark contrast area in 8(d). These features were characterized by subjecting selected pairs of lattice planes {(−1,−1,1) (1,1,−1) and (−1,1,−1) (1,−1,1)} to inverse Fourier transform (FFT) processing to produce corresponding filtered images shown

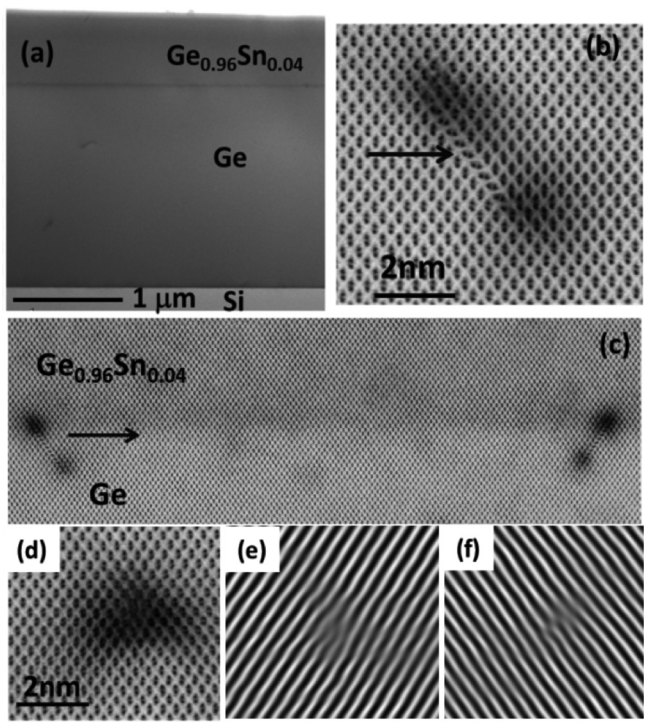

FIG. 8. XTEM high-resolution micrographs of a 700 nm-thick $Ge_{0.94}Sn_{0.04}$layer grown upon Si using a 1500 nm thick Ge buffer layer. (a) Image of the entire film structure showing good quality crystal morphology throughout. (b) STEM BF image of the interface (marked by an arrow) showing a magnified view of a single stacking fault site penetrating downward into the Ge buffer. These defects appear as dark contrast areas on the images at the film buffer-boundary on panel (c) and are well separated from one another by 42 nm. Typical Lomer dislocation accommodating the misfit strain is shown on panel (d). These features are identified by subjecting selected {111} planes to inverse FFT to generate the graphics on panels (e) and (f).

in panels 8(e) and 8(f). Both show two lattice planes terminating at the same point at the interface, as expected for this type of dislocation.

The presence of Lomers and stacking faults in the current samples represents a departure from typical relaxation behavior for Sn based alloys integrated on Si platforms and may be attributed to the less pronounced lattice mismatch of the epilayer and Ge template in the $Ge_{1-y}Si_y$/Ge system. Our atomic-scale structural observations are nevertheless consistent with similarly mismatched Si–rich $Si_{1-x}Ge_x$ films produced on Si wafers by low temperature CVD of Si and Ge hydrides. These films also showed high relaxation ratios combined with the generation of stacking faults crossing down into the Si substrate, as well as misfit dislocations localized at the interface plane as in our materials. Other factors that may play a significant role in controlling the relaxation behavior in our films is the low growth temperature and the heavy, high reactivity Ge/Sn sources employed in the deposition experiments. The latter enhance hydrogen desorption from the growth front, thus promoting organized assembly of planar films, as evidenced by AFM characterizations which showed low RMS roughness in the 1–3 nm range for large areas of $20\,\mu m \times 20\,\mu m$ throughout the surface. AFM also revealed crosshatch patterns presumably generated by dislocations penetrating to the surface or residual strain fields.

Elemental maps of the atomic columns were acquired along the [110] projection using element-selective EELS and STEM (see Fig. 9) in order to investigate the Sn and Ge distribution and gain insights into the local bonding configurations at the atomic scale. These experiments were performed on a JEOL 200 F ARM equipped with a GATAN Enfinium spectrometer. The EELS spectra were collected from $2 \times 2\,nm^2$ areas with spatial resolution of 0.12 nm and beam penetration distance of 60 nm. In all cases, the EELS scans revealed well defined ionization edges of Ge (L) and Sn (M) at 483 eV and 1217 eV, respectively. The spectra were then used to create atomic resolution maps of the lattice which show the Ge and Sn contributions in green and red color, respectively. The maps show the characteristic dumbbell-shaped dimers in the [110] projection for both elements, corroborating the notion that the Sn constituents are evenly distributed throughout the parent Ge lattice and occupy random substitution sites. Panel (d) is an overlay image of the Sn and Ge maps indicating a close alignment of the crystal columns, as evidenced by the uniform distribution of the red and green features within individual columns throughout the crystal pattern. In addition, we see no diffraction intensity above the background between the projected columns, indicating that the material is a pure, single-phase alloy devoid of precipitates and interstitials.

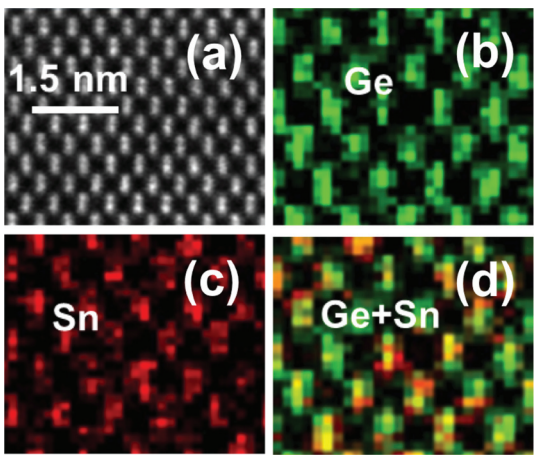

FIG. 9. EELS and STEM images of a $Ge_{0.96}Sn_{0.04}$ film (a) high-resolution image showing the area of the crystal analyzed by EELS. (b–c) individual EELS maps of Ge (green) and Sn (red) constituent atoms (d) composite map of Sn plus Ge illustrating a uniform distribution of the green and red features, indicating that Sn and Ge atoms occupy the same lattice.

V. OPTICAL PROPERTIES

PL measurements were carried out with the samples held at room temperature and illuminated with 200 mW of radiation generated from a continuous wave (CW) 980 nm laser focused to a 100 μm spot. The emitted light was collected by an $f = 140$ mm Horiba MicroHR spectrometer equipped with a 600 grooves/mm blazed at 2 μm. The spectrometer is fitted with a liquid nitrogen (LN_2) cooled extended InGaAs detector with a detection range of 1300–2300 nm. A 1400 nm long pass filter is employed to remove possible emission of visible radiation from the Si substrate. In spite of this filter, a clear 2nd order laser signal at 1960 nm is seen in all raw spectra and is subtracted from the data by fitting the laser peak with a Gaussian. The raw spectrum is further corrected to account for filter transmission and spectrometer response using calibration curves obtained from measurements of a tungsten lamp.

Figure 10 shows corrected PL spectra from selected $Ge_{1-y}Sn_y$/Ge/Si samples compared with $Ge_{1-y}Sn_y$/Si analogs with similar Sn concentrations and thickness, collected under identical conditions. The most striking feature in the spectra is the much stronger PL intensity from the samples grown on Ge-buffer layers. The intensity enhancements average one order of magnitude, and are assigned to reduced non-radiative recombination rates in the $Ge_{1-y}Sn_y$/Ge/Si films. As suggested above, there are two main sources of non-radiative recombination in $Ge_{1-y}Sn_y$ films: bulk-like defects, such as threading dislocations, and defects localized at the interface with Si, which are responsible for a very high recombination velocity at this interface.[45] Both sources of non-radiative recombination are suppressed in our $Ge_{1-y}Sn_y$/Ge/Si films: the bulk-like defect concentration is lower, as evidenced by the reduced widths of the XRD rocking curves, and the carriers are likely confined to the $Ge_{1-y}Sn_y$ layer, away from the Ge/Si interface, because the valence and conduction band offsets between $Ge_{1-y}Sn_y$ and Ge are of type I.[19] The separation between the two contributions will require systematic measurements and modeling of the PL intensity as a function of layer thickness for a fixed Sn concentration.

The increased intensity of the PL signal makes it far easier to study the detailed structure of the PL spectra, including the contributions from the direct and indirect edges. Unlike

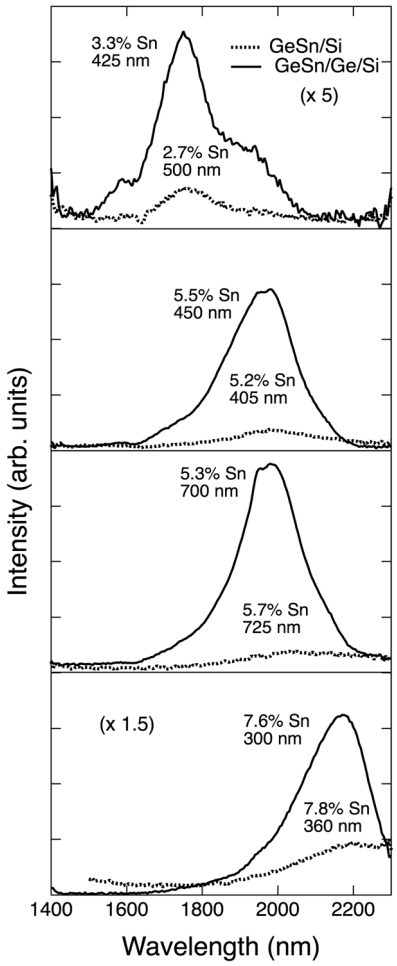

FIG. 10. Photoluminescence spectra from $Ge_{1-y}Sn_y$/Ge/Si and $Ge_{1-y}Sn_y$/Si counterpart films with similar Sn−concentration and thickness.

most semiconductors, in which PL arises from the lowest band gap, whether direct or indirect, in Ge one sees evidence for both direct and indirect gap emission.[46–48] This unique property reflects Germanium's peculiar band structure, in which the direct band gap is only 140 meV above the indirect edge. Even for very small thermal occupation of the conduction band minimum associated with the direct gap, the much higher oscillator strength of the direct optical transition leads to a signal that is comparable to the indirect gap emission, and in fact stronger if reabsorption effects are corrected for or eliminated, as in thin films. Figure 11 shows two examples of samples in which the direct and indirect edge are clearly visible. As discussed in prior work,[48,49] the indirect emission is fit with a simple Gaussian and the direct gap emission is fit with an Exponentially Modified Gaussian that accounts from the observed and expected asymmetry of the emission profile. The fit with these functions is indicated as dotted (direct gap) and dash-dotted (indirect gap) lines in the figure. From such fits, one can extract the energies of the direct and indirect band gaps in $Ge_{1-y}Sn_y$ alloys and study their compositional dependence. A detailed account will be presented elsewhere. Notice, however, that the separation between the direct and indirect emission decreases, and the direct gap emission intensity increases, as the Sn concentration is raised from 3% to 4.5%, approaching the concentration for which

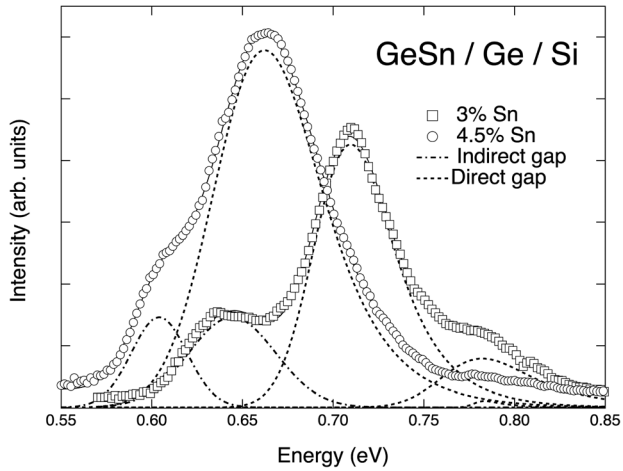

FIG. 11. Circles and squares show photoluminescence from two selected $Ge_{1-y}Sn_y$/Ge/Si samples. The solid line adjusted to the spectra is a fit with a combination of a Gaussian for the indirect gap emission and an EMG for the direct gap emissions from the $Ge_{1-y}Sn_y$ top layer and the Ge buffer. The dotted and dashed-dotted lines show the three components of the fit for the two samples.

the material transitions from indirect to direct-gap semiconductor.

VI. CONCLUSIONS

$Ge_{1-y}Sn_y$ films have been grown on Ge-buffered Si, and their structural and optical properties have been studied in detail and compared with measurements from similar films grown directly on Si substrates. Substantially lower defect levels are seen in films grown on Ge buffer layers, which make it possible to easily achieve film thicknesses close to 1 μm. At these thicknesses, we find very high levels of strain relaxation, as expected from theoretical simulations of the strain relaxation process. The elimination of compressive strains and the lower defect levels lead to dramatic improvement in the intensity of optical emission, suggesting that relaxed $Ge_{1-y}Sn_y$ films on Ge-buffered Si substrates are the most promising pathway to $Ge_{1-y}Sn_y$ lasers on Si. Our low temperature synthesis approach combined with the use of highly reactive Ge_3H_8 and SnD_4 sources provides access to both intrinsic and doped layers with compositions near the direct gap threshold, opening the door for subsequent development of the latter devices on Ge/Si(100) platforms.

ACKNOWLEDGMENTS

This work was supported by the Air Force Office of Scientific Research under contracts DOD AFOSR FA9550-12-1-0208. We would like to thank Dr. Federica Gencarelli (imec) and Professor Henry Cheng (National Taiwan University) for helpful correspondence and for sharing with us details of their growth data that allowed us to carry out our strain relaxation calculations.

[1]R. Roucka, J. Mathews, C. Weng, R. Beeler, J. Tolle, J. Menendez, and J. Kouvetakis, IEEE J. Quantum Electron. **47**(2), 213 (2011).
[2]G. He and H. A. Atwater, Phys. Rev. Lett. **79**(10), 1937 (1997).

[3]V. R. D'Costa, C. S. Cook, A. G. Birdwell, C. L. Littler, M. Canonico, S. Zollner, J. Kouvetakis, and J. Menendez, Phys. Rev. B **73**(12), 125207 (2006).
[4]J. Mathews, R. T. Beeler, J. Tolle, C. Xu, R. Roucka, J. Kouvetakis, and J. Menéndez, Appl. Phys. Lett. **97**(22), 221912 (2010).
[5]S. Takeuchi, Y. Shimura, T. Nishimura, B. Vincent, G. Eneman, T. Clarysse, J. Demeulemeester, A. Vantomme, J. Dekoster, M. Caymax, R. Loo, A. Sakai, O. Nakatsuka, and S. Zaima, Solid-State Electron. **60**(1), 53 (2011).
[6]B. Vincent, Y. Shimura, S. Takeuchi, T. Nishimura, G. Eneman, A. Firrincieli, J. Demeulemeester, A. Vantomme, T. Clarysse, O. Nakatsuka, S. Zaima, J. Dekoster, M. Caymax, and R. Loo, Microelectron. Eng. **88**(4), 342 (2011).
[7]M. Bauer, J. Taraci, J. Tolle, A. V. G. Chizmeshya, S.Zollner, D. J. Smith, J. Menendez, C. Hu, and J. Kouvetakis, Appl. Phys. Lett. **81**, 2992 (2002).
[8]J. M. Baribeau, T. E. Jackman, D. C. Houghton, P. Maigné, and M. W. Denhoff, J. Appl. Phys. **63**(12), 5738 (1988).
[9]L. Colace, G. Masini, F. Galluzzi, G. Assanto, G. Capellini, L. Di Gaspare, and F. Evangelisti, Solid State Phenom. **54**, 55 (1997).
[10]Z. Zhou, C. Li, H. Lai, S. Chen, and J. Yu, J. Cryst. Growth **310**(10), 2508 (2008).
[11]K. W. Shin, H.-W. Kim, J. Kim, C. Yang, S. Lee, and E. Yoon, Thin Solid Films **518**(22), 6496 (2010).
[12]Y. Yamamoto, P. Zaumseil, T. Arguirov, M. Kittler, and B. Tillack, Solid-State Electron. **60**(1), 2 (2011).
[13]B. Vincent, F. Gencarelli, H. Bender, C. Merckling, B. Douhard, D. H. Petersen, O. Hansen, H. H. Henrichsen, J. Meersschaut, W. Vandervorst, M. Heyns, R. Loo, and M. Caymax, Appl. Phys. Lett. **99**(15), 152103 (2011).
[14]H. Li, Y. X. Cui, K. Y. Wu, W. K. Tseng, H. H. Cheng, and H. Chen, Appl. Phys. Lett. **102**(25), 251907 (2013).
[15]A. L. Smirl, S. C. Moss, and J. R. Lindle, Phys. Rev. B **25**(4), 2645 (1982).
[16]E. Gaubas and J. Vanhellemont, Appl. Phys. Lett. **89**(14), 142106 (2006).
[17]R. Roucka, J. Mathews, R. T. Beeler, J. Tolle, J. Kouvetakis, and J. Menéndez, Appl. Phys. Lett. **98**(6), 061109 (2011).
[18]M. Oehme, E. Kasper, and J. Schulze, ECS J. Solid State Sci. Technol. **2**(4), R76 (2013).
[19]J. Menendez and J. Kouvetakis, Appl. Phys. Lett. **85**(7), 1175 (2004).
[20]F. Gencarelli, B. Vincent, J. Demeulemeester, A. Vantomme, A. Moussa, A. Franquet, A. Kumar, H. Bender, J. Meersschaut, W. Vandervorst, R. Loo, M. Caymax, K. Temst, and M. Heyns, ECS J. Solid State Sci. Technol. **2**(4), P134 (2013).
[21]R. Ragan and H. A. Atwater, Appl. Phys. Lett. **77**(21), 3418 (2000).
[22]J. Werner, M. Oehme, M. Schmid, M. Kaschel, A. Schirmer, E. Kasper, and J. Schulze, Appl. Phys. Lett. **98**(6), 061108 (2011).
[23]A. A. Tonkikh, V. G. Talalaev, and P. Werner, Semiconductors **47**(11), 1452 (2013).
[24]A. A. Tonkikh, C. Eisenschmidt, V. G. Talalaev, N. D. Zakharov, J. Schilling, G. Schmidt, and P. Werner, Appl. Phys. Lett. **103**(3), 032106 (2013).
[25]H. H. Tseng, H. Li, V. Mashanov, Y. J. Yang, H. H. Cheng, G. E. Chang, R. A. Soref, and G. Sun, Appl. Phys. Lett. **103**(23), 231907 (2013).
[26]G. Grzybowski, R. T. Beeler, L. Jiang, D. J. Smith, J. Kouvetakis, and J. Menéndez, Appl. Phys. Lett. **101**(7), 072105 (2012).
[27]L. R. Doolittle, Nucl. Instrum. Methods Phys. Res. B **9**(3), 344 (1985).
[28]R. Beeler, R. Roucka, A. Chizmeshya, J. Kouvetakis, and J. Menéndez, Phys. Rev. B **84**(3), 035204 (2011).
[29]Y. Ishikawa, K. Wada, D. D. Cannon, J. Liu, H.-C. Luan, and L. C. Kimerling, Appl. Phys. Lett. **82**(13), 2044 (2003).
[30]J. W. Matthews and A. E. Blakeslee, J. Cryst. Growth **27**, 118 (1974).
[31]D. C. Houghton, J. Appl. Phys. **70**(4), 2136 (1991).
[32]J. Menéndez, J. Appl. Phys. **105**(6), 063519 (2009).
[33]J. P. Hirth and J. Lothe, *Theory of Dislocations* (McGraw-Hill, New York, 1968), p.780.
[34]J. M. J. den Toonder, J. A. W. van Dommelen, and F. P. T. Baaijens, Modell. Simul. Mater. Sci. Eng. **7**(6), 909 (1999).
[35]H. J. McSkimin and P. Andreatch, J. Appl. Phys. **35**(11), 3312 (1964).
[36]D. L. Price, J. M. Rowe, and R. M. Nicklow, Phys. Rev. B **3**(4), 1268 (1971).
[37]N. Bhargava, M. Coppinger, J. Prakash Gupta, L. Wielunski, and J. Kolodzey, Appl. Phys. Lett. **103**(4), 041908 (2013).
[38]R. Hull, J. C. Bean, and C. Buescher, J. Appl. Phys. **66**(12), 5837 (1989).
[39]I. Yonenaga, M. Werner, M. Bartsch, U. Messerschmidt, and E. R. Werner, Phys. Status Solidi A **171**(1), 35 (1999).
[40]T. J. Gosling, S. C. Jain, and A. H. Harker, Phys. Status Solidi A **146**(2), 713 (1994).
[41]E. Kasper, N. Burle, S. Escoubas, J. Werner, M. Oehme, and K. Lyutovich, J. Appl. Phys. **111**(6), 063507 (2012).
[42]F. Gencarelli, private communication (2014).
[43]J. E. Ayers, J. Cryst. Growth **135**(1–2), 71 (1994).
[44]P. D. Healey, K. Bao, M. Gokhale, J. E. Ayers, and F. C. Jain, Acta Crystallogr. Sec. A **51**(4), 498 (1995).
[45]A. Trita, I. Cristiani, V. Degiorgio, D. Chrastina, and H. von Känel, Appl. Phys. Lett. **91**(4), 041112 (2007).
[46]J. R. Haynes, Phys. Rev. **98**(6), 1866 (1955).
[47]T. Arguirov, M. Kittler, and N. V. Abrosimov, J. Phys.: Conf. Ser. **281**, 012021 (2011).
[48]G. Grzybowski, R. Roucka, J. Mathews, L. Jiang, R. Beeler, J. Kouvetakis, and J. Menéndez, Phys. Rev. B **84**(20), 205307 (2011).
[49]J. D. Gallagher, C. Xu, L. Jiang, J. Kouvetakis, and J. Menéndez, Appl. Phys. Lett. **103**(20), 202104 (2013).